INTERNATIONAL JOURNAL FOR NUMERICAL METHODS IN FLUIDS, VOL. 25, 1207–1226 (1997)

EXPLICIT/IMPLICIT FLUID/STRUCTURE STAGGERED PROCEDURES WITH A STRUCTURAL PREDICTOR AND FLUID SUBCYCLING FOR 2D INVISCID AEROELASTIC SIMULATIONS

SERGE PIPERNO*

CERMICS, INRIA, F-06902 Sophia-Antipolis Cedex, France

SUMMARY

Field time integrators with second-order-accurate numerical schemes for both the fluid and the structure are considered for unsteady Euler aeroelastic computations. We show that if these schemes are simply coupled and used straightforwardly with subcycling, then accuracy and stability properties may be lost. We present new coupling staggered procedures where momentum conservation is enforced at the interface. This is done by using a structural predictor. Continuity of structural and fluid grid displacements is not satisfied at the fluid/structure interface. However, we show on a two-degree-of-freedom aerofoil that this new type of method has many advantages, e.g. accuracy of conservation at the interface and extended stability. The supersonic flutter of a flat panel is simulated in order to numerically prove that the algorithm gives accurate results with arbitrary subcycling for the fluid in the satisfying limit of 30 time steps per period of coupled oscillation. © 1997 John Wiley & Sons, Ltd.

Int. J. Numer. Meth. Fluids, **25**: 1207–1226 (1997)

No. of Figures: 16. No. of Tables: 2. No. of References: 21.

KEY WORDS: fluid/structure interaction; staggered procedure; subcycling; moving boundaries; structural predictor; panel flutter

1. INTRODUCTION

Fluid/structure interaction and especially aeroelasticity are fields where numerical simulation can be used to improve the physical understanding of coupled instabilities such as those appearing in aircraft[1] or suspended span bridges.[2] However, the direct, fully coupled solution is still out of reach. Actually, we have at our disposal complex, efficient and robust time integrators for both the structure and the fluid flow. The natural way to predict the aeroelastic behaviour of a flexible structure in a fluid flow would result from the coupling of methods for both decoupled fields.[3]

We consider here staggered procedures for the transient solution of coupled aeroelastic problems. In this type of algorithm the fluid and the structure are successively but not simultaneously time-integrated. The structure determines at least partially the fluid boundaries, whereas the fluid exerts a pressure force along the fluid/structure interface. Since the fluid domain boundaries are time-dependent, it becomes necessary to perform the integration of the fluid equations on a moving mesh. Among a number of existing methods we have chosen dynamic meshes[4] and finite volume methods based on the ALE formulation of the Euler equations.[5] Even if computational fluid dynamics (CFD)

*Correspondence to: S. Piperno, CERMICS, INRIA, F-06902 Sophia-Antipolis Cedex, France.

CCC 0271–2091/97/101207–20 $17.50

Received 18 March 1996
Revised 22 October 1996

and structural dynamics (SD) methods are accurate and efficient, the global coupling procedure is crucial. Recently, new partitioned procedures have been elaborated for coupled linear one-dimensional problems,[6] ensuring properties often verified by each method for both decoupled fields, e.g. stability and conservation.

In this paper these methods are adapted and extended to non-linear Euler two-dimensional aeroelastic cases and a new type of staggered procedure with a structural predictor is introduced, allowing us to obtain accuracy and robustness. These methods are tried on two test cases. The first physical problem consists of an NACA 0012 aerofoil oscillating in a transonic fluid flow. The second problem is the supersonic flutter of a flat panel with infinite aspect ratio. We use a second-order-accurate, implicit, unconditionally stable time scheme for the structure and an explicit second-order-accurate time scheme for the fluid. The fluid time step is limited by CFL-like stability conditions and fluid subcycling is desirable. It allows us to perform fewer structural integrations. A successful subcycling mixed with inter-field parallelism can significantly reduce the total solution time.[7]

The paper is organized as follows. In Section 2 we present the physical test cases. In Section 3 we present the whole set of CFD and CSD methods that we use for the resolution of decoupled fields. For the fluid we introduce the fluid grid motion algorithm, the ALE formulation of the Euler equations on this moving grid and the Godunov finite volume method based on a MUSCL-type second-order extension of Roe's approximate Riemann solver. For the structure we reformulate the structural equations into a matrix form in order to use a simple trapezoidal rule. The most original part of our contribution is reported in Section 4. We review some enhancements made on global algorithms that are necessary for the effective coupling of both fields. We start from the simplest staggered procedure.[8] We then add time averaging of the aeroelastic forces exerted on the structure and introduce a structural predictor. We discuss the role of the structural predictor in terms of global energy and momentum conservations. Finally, numerical results on supersonic panel flutter are presented and discussed in Section 5.

2. PHYSICAL PROBLEMS

2.1. *Oscillating aerofoil in transonic inviscid flow*

We are interested in the numerical simulation of a two-dimensional transonic inviscid flow around an oscillating NACA 0012 aerofoil. This case is a simplification of future three-dimensional test cases where the fluid domain surrounds the aircraft. This kind of simulation allows aircraft designers to know at a lower cost the characteristics of their wings/aeroplanes when they are coupled with the fluid flow.

Structural model

The aerodynamic surface of the aerofoil is assumed rigid. Only two degrees of freedom are given: the vertical displacement h and the rotation θ around the centre of rotation (Figure 1).

The equations for the evolution of h and θ can be written[8] in dimensionalized form as

$$m\ddot{h} + S_\theta\ddot{\theta} + c_h\dot{h} + k_h h = F_h, \qquad S_\theta\ddot{h} + I_\theta\ddot{\theta} + c_\theta\dot{\theta} + k_\theta\theta = F_\theta, \tag{1}$$

where m is the mass of the aerofoil, I_θ and S_θ denote the aerofoil inertial and static moments around the elastic centre respectively, c_h and c_θ are damping coefficients, k_h and k_θ are stiffness coefficients and F_h and F_θ are the lift and moment (around the elastic centre C located at $x_C = a_h b$) respectively exerted on the aerofoil by the fluid.

The structure is defined through non-dimensional numbers. They are listed in Table I along with three unit setting assumptions for mass, length and time.

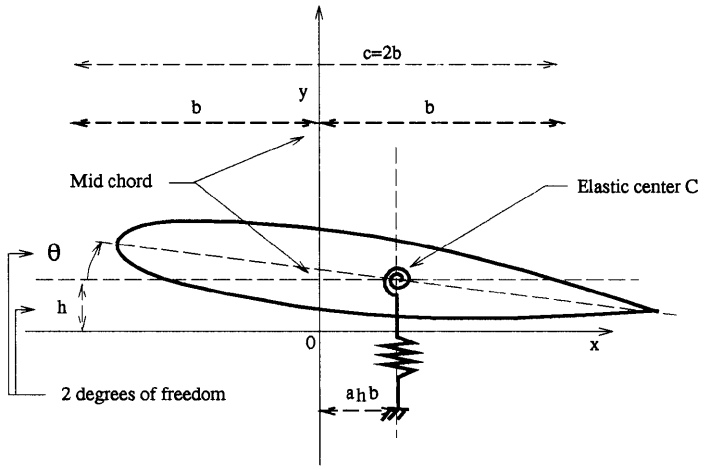

Figure 1. Two-degree-of-freedom aerofoil

All parameters in (1) are given as functions of the previous parameters by

$$\begin{aligned} b &= c/2, & \omega_h &= \lambda\omega_\theta, & k_h &= m\omega_h^2, & c_h &= 2\xi_h\omega_h m, \\ S_\theta &= mbx_\theta, & I_\theta &= mb^2\gamma_\theta^2, & k_\theta &= I_\theta\omega_\theta^2, & c_\theta &= 2\xi_\theta\omega_\theta I_\theta. \end{aligned} \tag{2}$$

The lift and moment coefficients F_h and F_θ are given by

$$F_h = \int_\Gamma p\vec{n}\cdot\vec{j}\,\mathrm{d}s, \qquad F_\theta = \int_\Gamma p(\vec{\mathrm{CM}}\times\vec{n})_z\,\mathrm{d}s, \tag{3}$$

where $p\vec{n}$ is the pressure force exerted by the fluid along the aerofoil Γ and M is a generic point on the profile (Figure 2).

Fluid model

We consider a perfect gas flowing around the aerofoil. The fluid satisfies the Euler equations in the time-dependent domain $\Omega(t)$ (Figure 3). $\Omega(t)$ is enclosed between the fixed far-field fluid boundary Γ_∞ and the oscillating aerofoil $\Gamma(t)$.

The vector of conservative variables, $W = (\rho, \rho u, \rho v, E)^{\mathrm{T}}$, where ρ, u, v and E respectively denote the density, the x- and y-velocity and the volumic total energy, is the solution of

$$\partial_t W + \partial_x \begin{pmatrix} \rho u \\ \rho u^2 + P \\ \rho uv \\ (E+P)u \end{pmatrix} + \partial_y \begin{pmatrix} \rho v \\ \rho uv \\ \rho v_2 + P \\ (E+P)v \end{pmatrix} = 0, \tag{4}$$

Table I. Unit setting assumptions and dimensionless coefficients

m	c	ω_θ	a_h	x_θ	γ_θ	ξ_h	ξ_θ	λ
1·0 kg	1·0 m	100 s^{-1}	−1	1·8	1·865	0	0	1

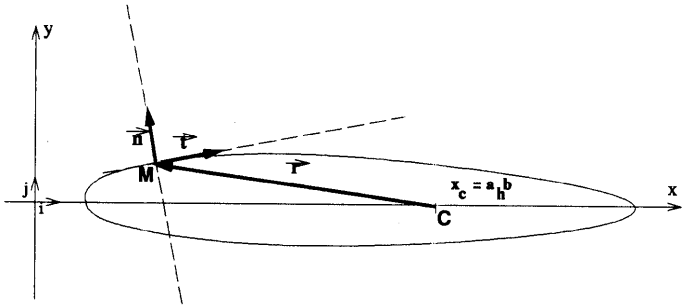

Figure 2. Detail of integration of F_h and F_θ

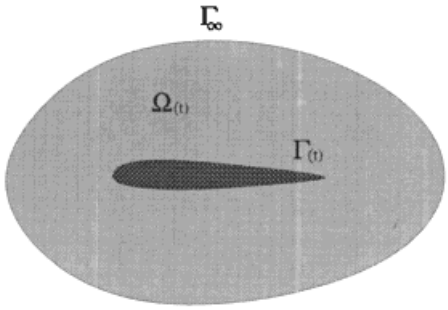

Figure 3. Time-dependent fluid domain $\Gamma(t)$

where the pressure P is given by the perfect gas law

$$P = (\gamma - 1)[E - \tfrac{1}{2}\rho(u^2 + v^2)], \quad \text{with } \gamma = 1{\cdot}4. \tag{5}$$

The boundary conditions for W are the following:

(a) $W = W_\infty$ along the far-field boundary Γ_∞
(b) $\vec{u} \cdot \vec{n} = \vec{u}_\Gamma \cdot \vec{n}$ along the aerofoil $\Gamma(t)$ (we have written $\vec{u} \equiv (u, v)^{\mathrm{T}}$ for the fluid velocity, $\vec{u}_\Gamma$ and $\vec{n}$ for the local interface speed and normal).

The definition of the problem is completed with the value of W_∞. It is a function of three user-specified non-dimensionalized parameters M_∞, V^* and μ as follows:

$$\begin{aligned} &\rho_\infty = \frac{m}{\pi\mu b^2}, \qquad u_\infty = b\omega_\theta V^*, \qquad v_\infty = 0, \\ &E_\infty = \left(\frac{1}{2} + \frac{1}{\gamma(\gamma - 1)M_\infty^2}\right)\rho_\infty u_\infty^2. \end{aligned} \tag{6}$$

We use $M_\infty = 0{\cdot}8$, $V^* = 5{\cdot}477$ and $\mu = 60$, which sets a problem of interest because the transonic $M_\infty = 0{\cdot}8$ is beyond the stability limit of the aerofoil and therefore flutter can appear. The density contours when flutter is reached are depicted in Figure 4. Two supersonic zones and two shocks below and above the aerofoil move back and forth as the aerofoil oscillates. This phenomenon produces negative damping.

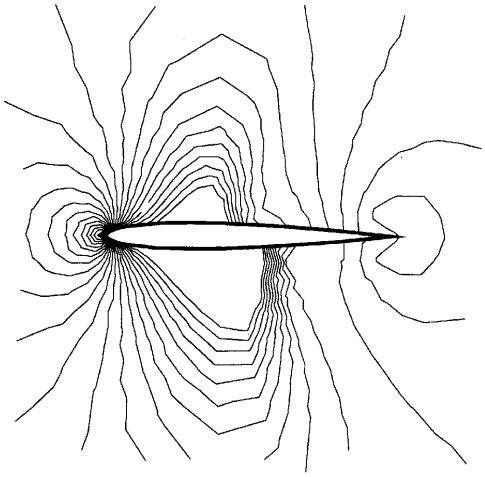

Figure 4. Non-dimensionalized density (minimum 0·7, maximum 1·3) around aerofoil at flutter

2.2. *Flat panel under supersonic inviscid flow*

We also test our methods on the more complex problems of a flat panel with infinite aspect ratio in a supersonic airstream. The surface skin panel has one side exposed to an airstream and the other side to still air. We try to simulate the supersonic flutter of this panel.[9,10]

Structural model

The panel (Figure 5) is given a length $L = 0{\cdot}5$ m, a uniform thickness $h = 1{\cdot}35 \times 10^{-3}$ m, a Young modulus $E = 7{\cdot}728 \times 10^{10}\,\mathrm{N\,m^{-2}}$, a Poisson ratio $v = 0{\cdot}33$ and a density $\rho_S - 2710\,\mathrm{kg\,m^{-3}}$. The panel is clamped at both ends ($x = 0$ and L). The pressure of the still air under the panel is equal to the fluid pressure at infinity, P_∞.

In order to have mass and stiffness matrices with large numbers on the diagonal, we use an actual two-dimensional modelization for the structure. The finite element formulation is based on a plane

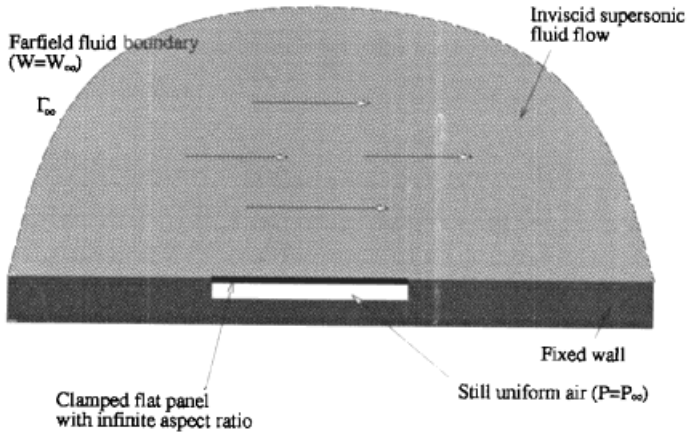

Figure 5. Flat panel with infinite aspect ratio

stress elastic model. The structure is discretized in N_x horizontal and N_y vertical quadrilateral isoparametric elements. Each mesh point is given two degrees of freedom (vertical and horizontal deflections). The mass and stiffness matrices of one quadrilateral isoparametric element are easily computed.[11] The quadrilateral isoparametric element has well-known drawbacks. It has quite poor accuracy and is easily subject to 'mesh locking' (decline of accuracy with shape distortion) when the aspect ratio of elements is very different from unity. Nevertheless, this element was chosen in order to generate complex structural matrices (like those obtained in real computations).

Finally, the fluid pressure forces are simply transferred from the fluid to the structure when both the fluid and structural meshes are matching. The computation of the applied pressure forces will be detailed later for the non-matching case.

Fluid model

W is the solution of the Euler equations (4) and (5) in the fluid domain $\Omega(t)$ enclosed between Γ_∞, the fixed wall and the clamped flat panel. The boundary conditions are the following:

(a) $W = W_\infty$ along the far-field fluid boundary Γ_∞; the state W_∞ is supersonic with no vertical velocity ($v = 0$) and is completely defined by the pressure $P_\infty = 25714\,\mathrm{Pa}$, the density $\rho_\infty = 0{\cdot}4\,\mathrm{kg\,m^{-3}}$ and the Mach number M_∞
(b) $v = 0$ along the fixed wall (slip condition)
(c) $\vec{u} \cdot \vec{n} = \vec{u}_\Gamma \cdot \vec{n}$ (slip condition on the moving boundary $\Gamma(t)$).

Instability

In this subsection we give a quick sketch of a simplified analytical study on the linear instability of the panel.[9] This analysis is based upon shallow shell theory and a first-order approximation of aerodynamic theory where the influence of three-dimensional aerodynamic effects is neglected (this approximation is valid for $M_\infty > 1{\cdot}6$).

When the structural vertical deflection X is very small, the fluid pressure forces on the panel can be approximated as a function of X and its derivatives. The global aeroelastic equation then reads

$$\rho_S h \frac{\partial^2 X}{\partial t^2} + \frac{Eh^3}{12(1-\nu^2)} \frac{\partial^4 X}{\partial x^4} = -\frac{\rho_\infty u_\infty^2}{\sqrt{(M_\infty^2 - 1)}} \frac{\partial X}{\partial x} - \frac{\rho_\infty u_\infty (M_\infty^2 - 2)}{(M_\infty^2 - 1)^{3/2}} \frac{\partial X}{\partial t}, \tag{7}$$

where u_∞ denotes the gas velocity at infinity. The boundary conditions for the deflection X (clamped panel) are

$$X(0) = X(L) = \frac{\partial X}{\partial x}(0) = \frac{\partial X}{\partial x}(L) = 0. \tag{8}$$

Frequencies for coupled modes are computed and the limit Mach number where an unstable coupled mode appears can be estimated with a resolution method of Houbolt.[12] For the present data an instability appears at $M_\infty = 2{\cdot}27$ with a pulsation $\omega = 462\,\mathrm{rad\,s^{-1}}$. The real part of the coupled flutter mode is clearly asymmetric (Figure 6) because of the action of the supersonic airstream. The point with the maximal amplitude is located near $x = 0{\cdot}35\,\mathrm{m}$.

This limit Mach number is used to test our numerical methods, since the exact solution is a perfect (neither damped nor amplified) oscillation. A glance at the results will tell us what amount of numerical damping our algorithms produce and whether or not they are stable.

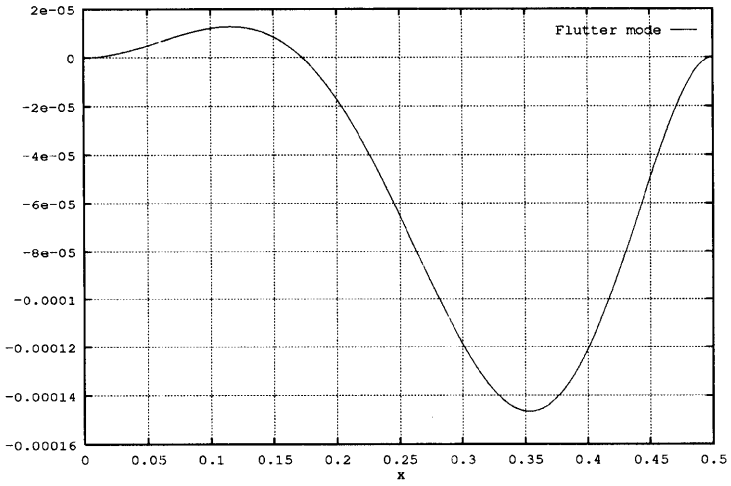

Figure 6. Vertical deflection for flutter mode (real part)

3. NUMERICAL METHODS

In this section we present the numerical methods used for each field, which are classical methods of CFD (even though the fluid domain is time-dependent) or CSD. Our most important contribution in this paper deals with the effective fluid/structure coupling and is presented in Section 4.

3.1. Numerical methods used for the fluid

We first present the spatial discretization and the grid moving/updating schemes we use. Once we have introduced the arbitrary Lagrangian–Eulerian (ALE) formulation of the Euler equations, we finish with the finite volume method used for the fluid on a dynamic mesh.

Spatial discretization: design and updating scheme

We assume that we have an initial unstructured triangulation $\Omega^h(0)$ of the fluid domain $\Omega(0)$. The boundary points of this triangulation are located either on the far-field boundary Γ_∞ (and they form the set Γ_∞^h) or on the aerofoil $\Gamma(0)$ (set $\Gamma^h(0)$). We describe here the updating scheme for the fluid mesh from time t_1 to time t_2. We assume that we know the location of the fluid/structure interface at time t_2. For the aerofoil problem we only need the values $\theta(t_2)$ and $h(t_2)$ of the two structural degrees of freedom at time t_2. For the panel problem we have to know the whole structural state at time t_2. The rest of $\Omega^h(t_2)$ is obtained via a method proposed by Batina[4] and generalized by Lesoinne and Farhat.[13] This method enables us to move the mesh with no addition or deletion of any vertex. Briefly, each edge ij (between vertices i and j) is given a stiffness (e.g. the inverse of its length). We seek the displacements $\vec{\delta}_i$ of all vertices from $\Omega^h(t_1)$ to $\Omega^h(t_2)$. The vertices get back to equilibrium when

$$\sum_{j\in N(i)} k_{ij}(\vec{\delta}_j - \vec{\delta}_i) = 0 \quad \text{for } i \in \Omega^h/(\Gamma^h \cup \Gamma_\infty), \tag{9}$$

where $N(i)$ is the set of vertices neighbouring i. The equation of displacements is solved with a Jacobi-type iterative method in which the displacements (inside the domain) are initialized with a linear prediction.

ALE formulation

We present here the arbitrary Lagrangian–Eulerian formulation of the Euler equations (4). This allows us to consider the classical Euler equations in a moving domain.[14] $\vec{\xi}$ and $\vec{x}$ respectively denote some mixed geometric co-ordinates and the laboratory co-ordinates. $\vec{\xi}$ plays the role of a moving frame of reference linked to the mesh $\Omega^h(t)$, i.e. the $\vec{\xi}$-co-ordinates of the vertices do not depend on time. Let us define the Jacobian J and the mesh speed $\vec{w}$ by

$$J = \det\left(\frac{\partial \vec{x}}{\partial \vec{\xi}}\bigg|_t\right), \qquad \vec{w} = \frac{\partial \vec{x}}{\partial t}|_{\vec{\xi}}. \tag{10}$$

The ALE formulation of the Euler equations reads

$$\frac{\partial (JW)}{\partial t}\bigg|_{\vec{\xi}} + J \operatorname{div}_{\vec{x}} \vec{\bar{F}} = 0, \tag{11}$$

where

$$\bar{F}_x = \begin{pmatrix} \rho\bar{u} \\ \rho u\bar{u} + p \\ \rho v\bar{u} \\ e\bar{u} + pu \end{pmatrix}, \qquad \bar{F}_y = \begin{pmatrix} \rho\bar{v} \\ \rho u\bar{v} \\ \rho v\bar{v} + p \\ e\bar{v} + pv \end{pmatrix}, \qquad \bar{u} = u - w_x, \qquad \bar{v} = v - w_y. \tag{12}$$

Integrating (11) on a fixed cell $C_{\vec{\xi}}$ (corresponding to the cell $C_{\vec{x}}$ moving in the laboratory co-ordinates) yields

$$\frac{\mathrm{d}}{\mathrm{d}t}\left(\int_{c_{\vec{x}}} W \mathrm{d}\vec{x}\right) + \int_{C_{\vec{x}}} \operatorname{div}_{\vec{x}} \vec{\bar{F}}\, \mathrm{d}\vec{x} = 0. \tag{13}$$

Numerical schemes

We use a finite volume formulation of the previous ALE Euler integral equation (13). For each vertex i, a median dual cell C_i is defined (Figure 7), ∂C_i denotes the boundary of this cell and $N(i)$ is the set of vertices j neighbouring i. ∂C_{ij} stands for $\partial C_i \cup \partial C_i$.

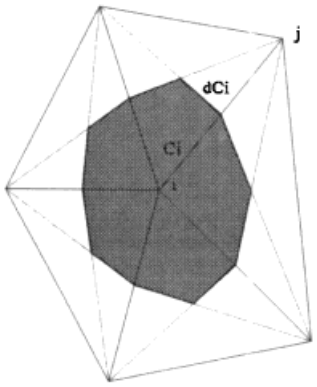

Figure 7. Cell and boundary for vertex i

The spatial scheme takes the form

$$(A_i W_i)_t + \sum_{j \in N(i)} \|\widetilde{\partial C_{ij}}\| \bar{\Phi}(W_i, W_j, \widetilde{\vec{\eta}_{ij}}) = 0, \tag{14}$$

where W_i is the averaged value of the field W in cell C_i, A_i is the area of cell C_i, $\widetilde{\partial C_{ij}}$ is a time average of ∂C_{ij} (of length $\|\widetilde{\partial C_{ij}}\|$ and normal $\widetilde{\vec{n}_{ij}}$ oriented from C_i to C_j) and $\bar{\Phi}$ is a numerical flux such that

$$\Delta t \|\widetilde{\partial C_{ij}}\| \bar{\Phi}(W_i, W_j, \widetilde{\vec{\eta}_{ij}}) \approx \int_{t^n}^{t^n + \Delta t} \left(\int_{\partial C_{ij}} \vec{\vec{F}} \cdot \vec{\eta}_{ij} \, \mathrm{d}\sigma \right) \mathrm{d}\tau. \tag{15}$$

We use a Godunov method based on Roe's approximate Riemann solver for the hyperbolic flux $\vec{\vec{F}}$. The numerical flux $\bar{\Phi}$ in (15) is taken as

$$\bar{\Phi}(W_i, W_j, \widetilde{\vec{\eta}_{ij}}) = \frac{\vec{\vec{F}}(W_i) + \vec{\vec{F}}(W_j)}{2} \widetilde{\vec{\eta}_{ij}} - |\tilde{\mathscr{A}}(W_i, W_j, \tilde{\eta}_{ij}) - (\widetilde{\vec{w}_{ij}} \cdot \widetilde{\vec{\eta}_{ij}})I| \frac{W_j - W_i}{2}, \tag{16}$$

where the matrix $\tilde{\mathscr{A}}(W_i, W_j, \eta \widetilde{\vec{\eta}_{ij}})$ is the Jacobian of the flux $\vec{\vec{F}} \cdot \widetilde{\vec{\eta}_{ij}}$ taken at Roe's average W_{ij} of the two states W_i and W_j.[11] The absolute value signs in (16) are common to all Roe-type methods (the matrix is diagonalized and absolute values of eigenvalues are computed).

N'Konga and Guillard[15] have discussed a choice for $\widetilde{\vec{w}_{ij}}$ and $\widetilde{\vec{\eta}_{ij}}$. This choice was advocated because it gives the Jacobian $\tilde{\mathscr{A}}(W_i, W_j, \widetilde{\vec{\eta}_{ij}})$ a propriety similar to Roe's linearization in the standard case.[16] It was also advocated by Farhat *et al.*[10] for conservation reasons. Indeed, if the location of the vertices are updated with the scheme

$$S_i^{n+1} = S_i^n + \Delta t \vec{w}_i^{n+1/2}, \tag{17}$$

where Δt is the current time step, then a uniform field $W \equiv W_0$ is conserved throughout the computation (i.e. the volume is also conserved) if the cell areas are updated with the same time scheme as in (14), i.e. according to

$$(A_i)_t + \sum_{j \in N(i)} \|\widetilde{\partial C_{ij}}\| (-\widetilde{\vec{w}_{ij}} \cdot \widetilde{\vec{\eta}_{ij}}) = 0. \tag{18}$$

The extension to a second-order accuracy follows the general idea of the MUSCL scheme initially developed by Van Leer[17] and adapted to unstructured finite elements by Fezoui.[18] We have chosen half-centred half-upwind gradients for the second-order extension. We refer the reader to References 11 and 16 for more details, especially on the treatment of boundary conditions.

Equation (14) can be seen as an ODE of the form $\partial_t(AW) + \Psi(W) = 0$. Time integration of this ODE is done using the following three-step explicit Runge–Kutta scheme with low storage:

$$\begin{aligned} W^{(0)} &= W^n, \\ W_i^{(k)} &= \frac{A_i^n}{A_i^{n+1}} W_i^{(0)} - \frac{1}{A_i^{n+1}} \frac{\Delta t}{4-k} \Psi(W^{(k-1)}), \quad k = 1, 2, 3, \\ W^{n+1} &= W^{(3)}. \end{aligned} \tag{19}$$

This time scheme is second-order-accurate. It is stable under a CFL-like condition on the fluid time step Δt.[19] Cell areas are always evaluated at the end of the current time step, which prevents actual second-order accuracy for the temporal scheme. However, tests were made which showed that this is not a source of significant inaccuracy.

3.2. Numerical methods used for the structure

Structural equations

For both model problems the linear structural equations are rewritten in matrix form as

$$M\ddot{X} + D\dot{X} + KX = F. \tag{20}$$

X still denotes the field of structural displacements. M, D and K respectively are the mass, damping and stiffness matrices. All three are symmetric and positive, M and K being positive definite. The trapezoidal rule can be used for (20) in both cases. In the following, A^n, V^n and X^n respectively denote approximations of $\ddot{X}(t^n)$, $\dot{X}(t^n)$ and $X(t^n)$. Using the time step $\Delta t = t^{n+1} - t^n$, the trapezoidal rule reads

$$\begin{aligned} &X^{n+1} = X^n + \Delta t V^{n+1/2}, \\ &V^{n+1} = V^n + \Delta t A^{n+1/2}, \\ &A^{n+1} \text{ such that } MA^{n+1} + DV^{n+1} + KX^{n+1} = F_{\mathrm{I}}^{n+1}, \end{aligned} \tag{21}$$

where $Z^{n+1/2}$ stands for $(Z^n + Z^{n+1})/2$ for any field Z. F_{I}^{n+1} is an estimate for the applied force at time t^{n+1}. This scheme is second-order-accurate and unconditionally stable. When $D = 0$, no numerical dissipation is added.

Pressure forces

We discuss here some choices concerning the input force F_{I}^{n+1}. If the pressure force on the structure at time t^{n+1} is not known, we have to use an estimate. If we use a subcycled coupling scheme, then we have to choose the pressure force we use (since we have computed these forces at several different times). Actually, the structural integration depends a lot on the general coupling procedure. The energy exchange at the fluid/structure interface depends on the time interpolation used.

Geometrically, some choices have to be made. In the case of the aerofoil the generalized forces detailed in (3) are integrated straightforwardly along Γ^h. For the panel flutter simulation the fluid and structural meshes are not matching at the fluid/structure interface. Linear matching interpolations are used (Figure 8). More precisely, the pressure $P_{\mathrm{F}\to\mathrm{S}}$ applied to a structural point is the barycentric weighted average of the neighbouring fluid pressures P_{L} and P_{R}. Reciprocally, the displacement $X_{\mathrm{F}\to\mathrm{S}}$ of a fluid grid point at the interface is the barycentric weighted average of the neighbouring structural displacements X_{L} and X_{R}.

4. CONSTRUCTION OF EFFICIENT STAGGERED PROCEDURES

In this section we review the fine points of the actual coupling of the fluid and the structure. Some of the methods presented here have been derived from one-dimensional studies.[20] We consider in this section the aerofoil simulation. Since each computation is inexpensive, we can make a lot of numerical tests. In Section 5 we shall verify the accuracy and efficiency of the constructed staggered procedures on the considerably more complex simulation of panel flutter.

Throughout this section we assume that fluid subcycling is desirable (which is the case indeed). We would like to perform fewer structural time integrations (with a larger time step) than fluid time integrations. This can lead to important savings in computational costs.[6] Therefore we keep in mind that we would like the maximum subcycling factor $n_{\mathrm{F/S}}$ (number of fluid subcycles per structural time integration) with the same accuracy.

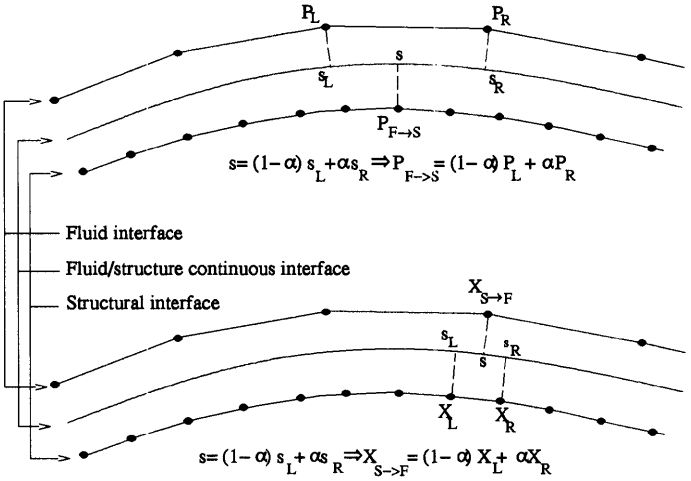

Figure 8. Interpolations at interface for non-matching grids

We use a fluid unstructured grid of 2280 vertices (120 vertices on the aerofoil) and 4320 triangles. For all simulations the initial fluid flow is the steady flow around the structure with $h = \theta = 0$. At time $t = 0$ the structure is given a vertical speed perturbation ($\dot{h} = 3{\cdot}42\,\mathrm{m\,s^{-1}}$, $\dot{\theta} = 0$).

4.1. Choice for the pressure forces

Let us begin with the simplest staggered procedure. One time integration of Δt_S is performed as follows.

1. Compute the generalized forces F in (1).
2. Perform a structural time integration (21) of Δt_S with $F_I^{n+1} = F$.
3. Update the mesh displacements on Γ and construct a new fluid grid as in (9).
4. Compute the grid velocities as in (17).
5. Perform as many fluid time steps (19) as necessary to complete the time step Δt_S.

We notice that continuity of the structure and fluid grid displacements is enforced at the end of a global time step. However, continuity of both displacements and velocities can only be achieved with an offset staggered procedure.[21]

Several choices are possible for the pressure forces of substep 1, depending on what kind of time interpolation is used. The results for the aerofoil rotation θ (in degrees) computed with two different choices are compared with a reference result obtained with no subcycling and a very small time step (Figure 9). The *previous* curve corresponds to $F = F^n$. The *averaged* curve corresponds to

$$F = \bar{F}^{n=1/2} \equiv \frac{1}{\Delta t_S} \sum_{k=1}^{n_{F/S}} \Delta t_{F_k} F_k^{n-1} \tag{22}$$

where the summation is extended over all subcycles, F_k^{n-1} being the pressure forces computed before the kth subcycle in the previous time step. For this test we have taken $\Delta t_S = 8{\cdot}76 \times 10^{-}4\,\mathrm{s}$. The subcycling factor is $n_{F/S} = 60$. We see that the choice for F has an obvious influence on the numerical results. We guess why the second method is worse that the first one: the computed value for F is roughly close to $F(t^{n-1/2})$ (and in the case of the *previous* curve it would be $F(t^n)$). Anyway, both

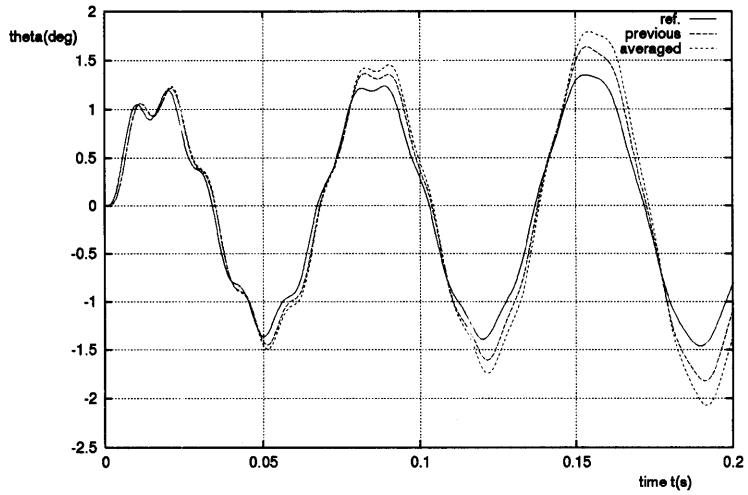

Figure 9. Aerofoil rotation with different pressure forces

schemes give results different from the reference curve. These preliminary results show that importance of the choice for the pressure input forces.

4.2. *Introduction of a structural predictor*

Staggered procedures using a structural predictor were recently introduced and advocated.[11] In short, they allow one to reduce considerably the energy conservation errors. The general idea is simple: assume one can construct with good accuracy a prediction of the state of the structure at the end of the *next* time step, then one should perform the three last steps of Section 4.1 and finish with the actual time integration of the structure. The new staggered procedure reads as follows.

1. Compute a prediction $\widetilde{X^{n+1}}$ for the structural displacement after the current time step.
2. Update the mesh displacements on Γ and construct a new fluid grid as in (9).
3. Compute the grid velocities as in (17).
4. Perform as many fluid time steps (19) as necessary to complete the time step Δt_S.
5. Compute some input forces F in (1).
6. Perform a structural time integration (21) of Δt_S with $F_I^{n+1} = F$.

At the end of a time step, continuity of the structural and fluid grid displacements at the fluid/structure interface is *a priori* not satisfied unless the structural predictor is perfect. As a first test we try the first-order predictor for the structural displacement.

$$\widetilde{X^{n+1}} = X^n + \Delta t_S V^n. \tag{23}$$

For the input forces F of substep 5 we simply use F^{n+1}. Because the fluid was time-integrated first, this information is *available*. This is one of the most remarkable differences from a staggered procedure without a structural predictor. As a matter of fact, these simple tricks are sufficient to obtain a result closer to the reference curve than the most accurate staggered procedure with no predictor, reported earlier as 'previous' (Figure 10). These results were obtained with $\Delta t_S = 8{\cdot}76 \times 10^{-4}$ s and $n_{F/S} = 60$.

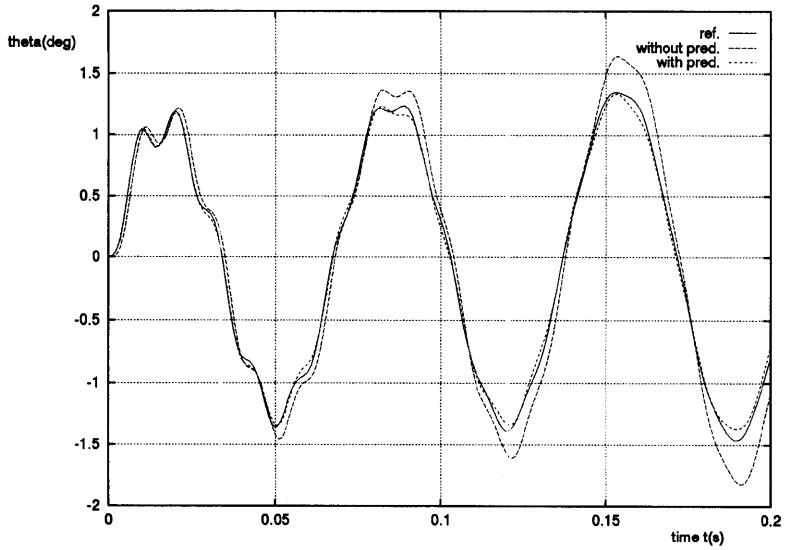

Figure 10. Aerofoil rotation with/without a structural predictor

4.3. Role of the structural predictor

We can wonder what is the influence of the structural predictor on the accuracy and stability of the staggered procedure. We have compared the first-order predictor (23) with three more accurate predictors. The first two are linear predictors and read

$$\widetilde{X^{n+1}} = X^n + \Delta t_S(1{\cdot}5V^n - 0{\cdot}5V^{n-1}), \tag{24}$$

$$\widetilde{X^{n+1}} = X^n + \Delta t_S V^n + \frac{\Delta t_S^2}{2} A^n. \tag{25}$$

The third one is the result of a numerical integration of the structure with F^n, i.e.

$$\begin{aligned} \widetilde{X^{n+1}} &= X^n + \frac{\Delta t_S}{2}(V^n + \widetilde{V^{n+1}}), \\ \widetilde{V}^{n+1} &= {}^n + \frac{\Delta t_S}{2}(A^n + \widetilde{A}^{n+1}), \\ \widetilde{A^{n+1}} &\text{ such that } M\widetilde{A^{n+1}} + D\widetilde{V^{n+1}} + K\widetilde{X^{n+1}} = F^m. \end{aligned} \tag{26}$$

We have made tests with up to 76 structural time steps per period of coupled oscillation (denoted by T_C in the sequel). The time step Δt_S is rather small but not negligible compared with T_C. The results are almost identical. For larger structural time steps the first predictor (24) is the most accurate, stable and inexpensive. However, in some cases where an implicit fluid solver is used (with a large fluid time step), some iterations based on the same principle as (26) can be very efficient.

4.4. Energy conservation

We discuss here the origin of the enhanced efficiency (accuracy and stability) of the staggered procedure with a structural predictor. Our discussion is based on energetic considerations and some elements of demonstration are given 'with the hands'. As a matter of fact, we only consider energetic

exchanges through an element of the fluid/structure interface (anyway, we do not discuss here some fine points of the spatial scheme but of the global procedure).

If the fluid is subcycled, then (the reader can check that) the energy received by the fluid through a structural boundary element is roughly given by

$$\Delta E_{\mathrm{F}} = -\sum_{k=1}^{n_{\mathrm{F/S}}} \Delta t_{\mathrm{F}_k} F_k^n w_k^n,$$

where w_k^n is the boundary velocity during the kth subcycle. We assume that w is constant through all subcycles ($w = w^{n+1/2}$). Defining $F^{n+1/2}$ as in (22) yields

$$\Delta E_{\mathrm{F}} = -\bar{F}^{n+1/2} \Delta t_{\mathrm{S}} w^{n+1/2}. \tag{27}$$

On the other hand, the energy received by the structure through a time integration with the trapezoidal rule is

$$\Delta E_{\mathrm{S}} = \frac{F_{\mathrm{I}}^n + F_{\mathrm{I}}^{n+1}}{2} \Delta t_{\mathrm{S}} V^{n+1/2},$$

where F_{I}^{n+1} is the input of the trapezoidal rule for the step $t^n \to t^{n+1}$. Finally, the total amount of energy *numerically created*, $\Delta E \equiv \Delta E_{\mathrm{F}} + \Delta E_{\mathrm{S}}$, is

$$\Delta E = \Delta t_{\mathrm{S}} \left[\left(\frac{F_{\mathrm{I}}^n + F_{\mathrm{I}}^{n+1}}{2} \right) V^{n+1/2} - \bar{F}^{n+1/2} w^{n+1/2} \right]. \tag{28}$$

At the same time, the amount of momentum *numerically created* by the staggered procedure is

$$\Delta Q = \Delta t_{\mathrm{S}} \left(\frac{F_{\mathrm{I}}^n + F_{\mathrm{I}}^{n+1}}{2} - \bar{F}^{n+1/2} \right). \tag{29}$$

Let us now consider a typical staggered procedure with no structural predictor. By construction, the trapezoidal rule yields $w^{n+1/2} = V^{n+1/2}$. The input force F_{I}^{n+1} is necessarily outdated, since $\bar{F}^{n+1/2}$ is unavailable. Besides, it is very difficult to find a good predictor for $\bar{F}^{n+1/2}$ (because the fluid time scale is smaller) in order to have a limited amount of momentum or energy created. Therefore a staggered procedure with no structural predictor will not have a large stability and accuracy domain.

In contrast, for a staggered procedure with a structural predictor, $\bar{F}^{n+1/2}$ *is available* when the structure is time-integrated from t^n to t^{n+1}. Let us define the matching error ε^n by $\varepsilon^n = \tilde{X}^n - X^n$. Taking $F_{\mathrm{I}}^{n+1} = 2\bar{F}^{n+1/2} - F_{\mathrm{I}}^n$ yields

$$\Delta Q = 0, \qquad \Delta E = \bar{F}^{n+1/2} (\varepsilon^{n+1} - \varepsilon^n). \tag{30}$$

The reader can notice that the use of a structural predictor induces an exact exchange of forces between the fluid and the structure at the interface. Moreover, (30) shows that the error on the energy exchange is controlled by the accuracy of the structural predictor. The staggered procedure is also flexible, since no definite type of predictor is requested.

We now test several choices for the input forces F_{I}^{n+1} of the trapezoidal rule for staggered procedures with a structural predictor. The rotations of the aerofoil computed with different inputs ($\Delta t_{\mathrm{S}} = 8{\cdot}76 \times 10^{-4}\,\mathrm{s} \approx T_{\mathrm{C}}/80$ and $n_{\mathrm{F/S}} = 60$) are compared with the reference result (Figure 11).

We tested the following inputs:

$$\begin{aligned} \text{averaged forces} \quad & F_{\mathrm{I}}^{n+1} = \bar{F}^{n+1/2}, \\ \text{last forces} \quad & F_{\mathrm{I}}^{n+1} = F^{n+1}, \\ \text{corrected forces} \quad & F_{\mathrm{I}}^{n+1} = 2\bar{F}^{n+1/2} - F_{\mathrm{I}}^n. \end{aligned} \tag{31}$$

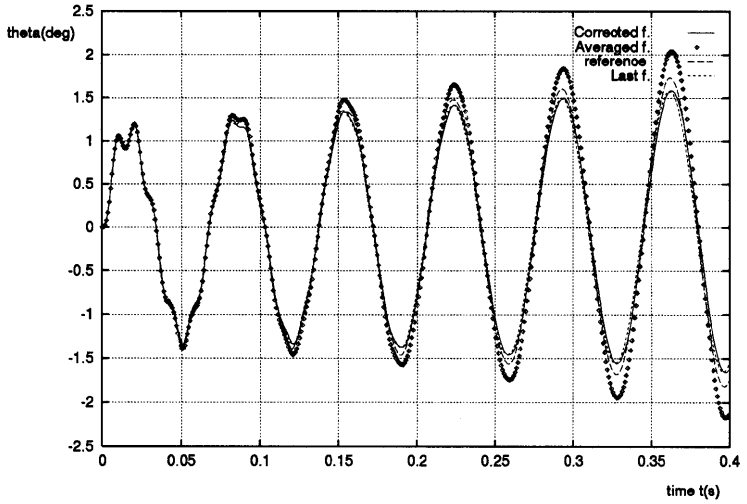

Figure 11. Energy conservation for different input forces

The results with *averaged forces* is not really good. The amplification of the flutter has changed. This was clearly foreseen by (28). *Last forces* give a much better result. However, tests with larger time steps showed that the resulting staggered procedure is quickly unstable ($\Delta t_S = T_C/70$ seems to be a limit). Finally, *corrected forces*—which imply exact momentum conservation—give a slightly better result than the preceding one. Moreover, the resulting staggered procedure happens to be stable up to $\Delta t_S = T_C/30$.

4.5. Grid motion and subcycling

In the preceding sections we have only considered grid motions with a constant speed during each global time step. Actual mesh motions are only computed before each global time step (with Jacobi iterations on (9)). Before each fluid time step, grid point locations are simply linearly time-interpolated, which saves some computational time. However, finite volume geometric data have to be fully updated. For each structural time step we compute once and for all subcycles the mesh speeds. This would not have been the case if we had chosen some more accurate interpolation of the grid point locations. However, Farhat *et al.*[10] confirm that the use of a parabolic or linear path for the fluid mesh during subcycles gives no significantly different results.

This might be different for cases where very few time steps are used for each coupled period of oscillation: the structural speed could vary a lot from one time step to the next and the use of a linear path for the fluid mesh could induce some additional numerical diffusion (due to the difference between the fluid velocity and the mesh speed at the fluid/structure interface during the first fluid subcycles of a global time step.)

5. APPLICATION TO PANEL FLUTTER SIMULATION

In this section we apply the previous enhancements to the numerical simulation of panel flutter described in Section 2.2. We first perform some computations based upon shallow shell theory. We have used a finite difference discretization of (7) with 299 points. The total fluid unstructured grid is made of 1654 vertices and 2936 triangles. For all these simulations we use second-order fluxes for the resolution of the Euler equations, along with the explicit Runge–Kutta time integrator (19). We use a Courant number equal to 1·4, which is within the stability domain of the fluid time integrator.

As a reference computation we first use a structural time step $\Delta t_S = 1{\cdot}23 \times 10^{-6}$ s, which induces no subcycling in the fluid. Compared with the first period of the panel, this time step is very small (remember that the period for the first structural mode is $T_1 = 31{\cdot}9$ ms, which yields $T_1/\Delta t_S = 25{,}900$!). The initial condition for the problem is the following. We compute a steady state flow around the structure, which is perturbed along its second mode.[6] Then the structure is given back the ability to move and the simulation starts. With $M_\infty = 2{\cdot}23$ the oscillations go on with no amplification or damping after a transient time (Figure 12). Instability is just reached and this gives foundation to the following discussion on the numerical properties of our method.

Numerically, we found the limit Mach number $\bar{M}_\infty = 2{\cdot}23$, which is in good agreement with the theoretical $\bar{M}_\infty = 2{\cdot}27$. We also find numerically that the flutter pulsation is $\bar{\omega} = 452\,\mathrm{rad\,s^{-1}}$, which is also in good agreement with the theoretical $\bar{\omega} = 462\,\mathrm{rad\,s^{-1}}$. Throughout this section, T_C denotes the coupled period of oscillation at flutter ($T_C = 13{\cdot}9$ ms). These slight discrepancies might be linked to the relative coarseness of the fluid mesh. This first computation will stand as a reference in the sequel.

We now test the staggered procedures with a structural predictor. We use the corrected forces (31) and a constant mesh speed during subcycles. We choose a structural time step $\Delta t_S = 0{\cdot}2\,\mathrm{ms} \approx T_C/70$. This gives a subcycling factor $n_{S/F} = 161$. We have plotted (Figure 13) the mass product of the displacement field X with the second structural mode (i.e. $X_2^T MX$) for the predictors (24) and (25). The predictor (25) is unstable with this time step. In contrast, the predictor (24) is stable and gives results in very good agreement with the reference curve.

For the predictor (24), bigger subcycling factors and structural time steps were considered (Figure 14). The method is perfectly acceptable for $\Delta t_S = 0{\cdot}4\,\mathrm{ms} \approx T_C/35$ ($n_{F/S} = 322$), but for $\Delta t_S = 0{\cdot}6\,\mathrm{ms} \approx T_C/23$ ($n_{F/S} = 483$) we have a rather poor definition of coupled oscillations. The scheme appears to be slightly inaccurate and unstable, as could be predicted.

In order to check whether our algorithm goes on well with a lot of degrees of freedom, we go back to the quadrilateral isoparametric finite element formulation of the plane stress elastic model of Section 2.2. We use 2221 points on the length and seven points on the height of the panel. This makes 31,094 structural degrees of freedom. With these data the aspect ratio for the elements is perfect, so no mesh locking appears. We use skyline storage for the matrices, which reduces the problem to a

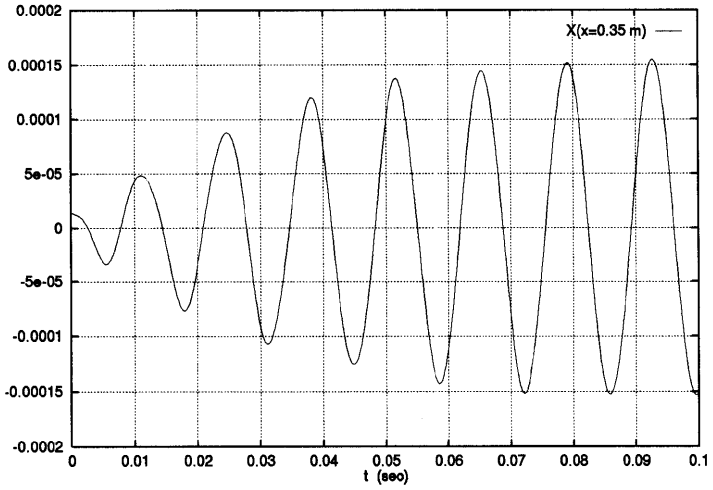

Figure 12. Vertical deflection at $x = 0{\cdot}35$ m—reference computation

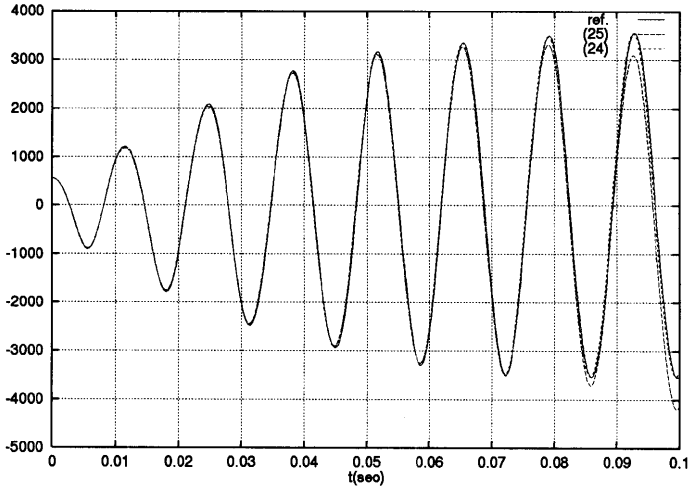

Figure 13. $X_2^T MX$ with different predictors ($n_{S/F} = 161$)

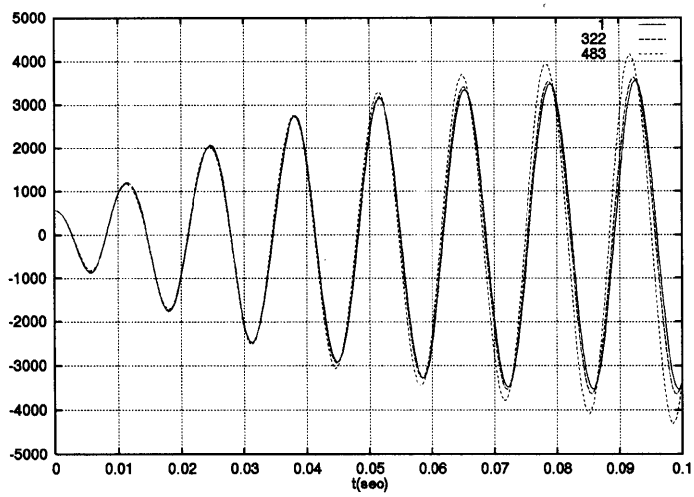

Figure 14. $X_2^T MX$ with predictor (24) and different subcycling factors $n_{S/F}$

million terms. This fine discretization is not needed for accuracy; we have designed this structural mesh in order to emphasize the computational time that can be saved with an efficient fluid subcycling.

A reference computation with a small time step Δt_S and no fluid subcycling shows that flutter appears just under $M_\infty = 2{\cdot}24$. The aim of an industrial simulation could be the determination of the flutter limit for this structure. Our point is to prove that our staggered procedures with fluid subcycling allow an accurate determination of the limit Mach number. Therefore we test our staggered procedure with the predictor (24) and corrected forces (31) for different Mach numbers.

We first perform computations with $M_\infty = 2{\cdot}24$ (Figure 15). The curve with $\Delta t_S = 0{\cdot}4\,\text{ms} \approx T_C/35$ compares well with the reference curve. In contrast, the curve with $\Delta t_S = 0{\cdot}6\,\text{ms} \approx T_C/23$ is inaccurate. Thirty time steps per period of coupled oscillation seems to be the accuracy and stability

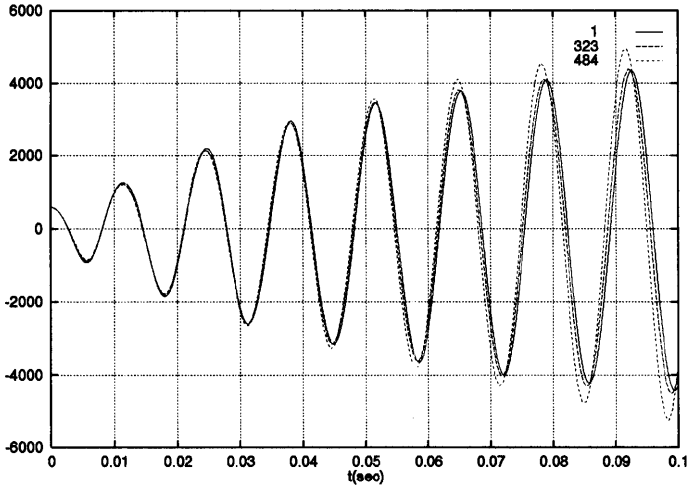

Figure 15. $X_2^T MX$ with several subcycling factors $n_{S/F}$ at $M_\infty = 2{\cdot}24$

limit for our algorithm, which is rather reasonable. We then make similar computations with $M_\infty = 2{\cdot}23$ (Figure 16). Again the same conclusions on the accuracy of the staggered procedure hold.

Moreover, the mass product curves (with no subcycling or with $\Delta t_S \approx T_C/35$) are slightly damped at $M_\infty = 2{\cdot}23$ and amplified at $M_\infty = 2{\cdot}24$. This shows numerically that the stability of the proposed staggered procedure with a structural predictor is not a consequence of the excessive production of numerical damping. On the contrary, this procedure allows us to detect that the flutter Mach number lies in [2·23; 2·24]. In addition, the procedure is stable and accurate with heavy fluid subcycling up to $n_{S/F} = 323$ and a global time step $\Delta t_S \approx T_C/35$.

The costs of the previous computations (made on a Cray Y-MP2E/232) are listed in Table II. In our tests the vectorized versions of the fluid procedures are notably more efficient than the structural

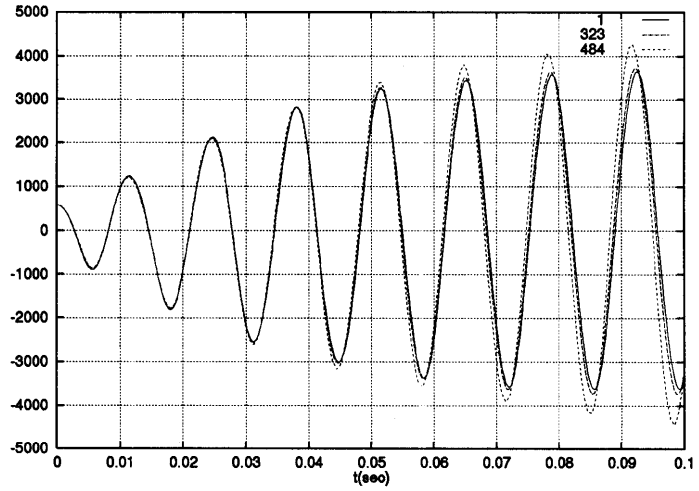

Figure 16. $X_2^T MX$ with several subcycling factors $n_{S/F}$ at $M_\infty = 2{\cdot}23$

Table II. Computatational cost and performance for different fluid subcycling factors

$n_{S/F}$	CPU time (h)	Mflops
1	5·48	136
4	2·54	143
41	1·60	153
81	1·54	154
162	1·51	155
323	1·49	156

procedures, because a non-vectorized skyline solver is used in our computations. However, subcyling can lead to dramatic savings when the structure is actually complex and time-consuming.

6. CONCLUSIONS

In this paper we introduced staggered procedures with a structural predictor for fluid/structure interaction simulations. We considered partitioned procedures where the structural time scheme is implicit and the fluid time integrator is explicit. In this particular context where fluid subcycling is desirable, these staggered procedures are accurate, stable and efficient.

Because of the use of a structural predictor, the proposed procedures do not satisfy continuity of the structural and fluid grid displacements/velocities at the fluid/structure interface. However, they allow an exact numerical exchange of momentum through the moving interface. Moreover, the energy artificially created because of staggering is controlled by the accuracy of the predictor used for the structural displacement at the end of the current time step. This prediction is corrected by the actual integration of the structure using a corrected time-averaged fluid pressure force.

The most stable and accurate staggered procedure with a structural predictor proposed in this paper was used to determine the supersonic flutter limit of a flat panel. The flutter limit was successfully located in the very sharp interval [2·23; 2·24]. This shows numerically that the procedure is stable and accurate, even under heavy fluid subcycling. It produces no numerical damping if the number of structural time steps per period of coupled oscillation is at least 30, which is more or less the weakest reasonable condition that could be imagined for this kind of staggered procedure.

The first results presented here are very promising, since heavy subcycling can reduce dramatically the computational cost of numerical simulations with complex structures. Besides, this quite general staggering algorithm can be adapted to implicit/implicit partitioned procedures. Extensions to more complex configurations in two and three dimensions are currently in progress.

ACKNOWLEDGEMENTS

We thank the Conseil Régional of Provence–Alpes–Côte d'Azur which provided computational time on the computer Cray Y-MP2E/232 of the Institut Méditérranéen de Technologie. We thank the team SINUS of INRIA and particularly A. Dervieux and S. Lantéri for providing us with all the necessary non-vectorized procedures for the fluid.

REFERENCES

1. G. P. Guruswamy, 'Interactions of fluids and structures for aircraft applications', *Comput. Struct.*, **30**, 1–13 (1988).
2. R. H. Scanlan, 'On the state of stability considerations for suspended-span bridges under wind', *Proc. IUTAM–IAHR Symp.*, Karlsruhe, 1979, pp. 595–618.
3. G. P. Guruswamy, 'Integrated approach for active coupling of structures and fluids', *AIAA J.*, **27**, 788–793 (1989).

4. J. T. Batina, 'Unsteady Euler airfoil solutions using unstructured dynamic meshes', *AIAA J.*, **28**, 1381–1388 (1990).
5. J. Donea, S. Giuliani and J. P. Halleux, 'An arbitrary Lagrangian Eulerian finite element method for transient dynamic fluid-structure interactions', *Comput. Meth. Appl. Mech. Engng.*, **33**, 689–723 (1982).
6. S. Piperno, C. Farhat and B. Larrouturou, 'Partitioned procedures for the transient solution of coupled aeroelastic problems', *Comput. Meth. Appl. Mech. Engng.*, **124**, 79–112 (1995).
7. C. Farhat, M. Lesoinne, P. Stern and S. Lantéri, 'High performance solution of 3D nonlinear aeroelastic problems via parallel partitioned algorithms: methodology and preliminary results', *J. Comput. Syst.*, in press.
8. S. Lanteri and C. Farhat, 'Rapport de recherche aéroélasticité. 3ème Partie: Mouvements de maillages et étude numérique sur des écoulements non visqueux', *Contrat DRET/AMDBA/PGSoft/INRIA*, 1993.
9. R. L. Bisplinghoff, H. Ashley and R. L. Halfman, *Aeroelasticity*, Addison-Wesley, Reading, MA, 1957.
10. C. Farhat, M. Lesoinne and N. Maman, 'Mixed explicit/implicit time integration of coupled aeroelastic problems: three field formulation, geometric conservation and distributed solution', *Int. j. numer. meth. fluids*, **21**, 807–835 (1995).
11. S. Piperno, 'Simulation numérique de phénomènes d'interaction fluide–structure', *Ph.D. Thesis*, Ecole Nationale des Ponts et Chaussées, 1995.
12. J. C. Houbolt, 'A study of several aerothermoelastic problems of aircraft structures', *Mitteilung aus dem Institut für Flugzeugstatik und Leichtbau 5*, ETH, Zurich, 1958.
13. M. Lesoinne and C. Farhat, 'Stability analysis of dynamic meshes for transient aeroelastic computations', *AIAA paper 93-3325*, 1993.
14. S. Piperno, 'Numerical methods used in aeroelasticity simulations', *Rap. Rech. CERMICS 92-5*, 1992.
15. B. N'Konga and H. Guillard, 'Godunov type method on non-structured meshes for three-dimensional moving boundary problems', *INRIA RR-1883*, INRIA Sophia-Antipolis, 1993.
16. S. Lanteri and C. Farhat, 'Rapport de recherche aéroélasticité. 2ème Partie: Etude bibliographique et analyse des méthodes', Contrat DRET/AMDBA/PGSoft/INRIA, 1992.
17. V. Van Leer, 'Towards the ultimate conservative difference scheme. V: A second-order sequel to Godunov's method', *J. Comput. Phys.*, **32**, 361–370 (1979).
18. L. Fezoui, 'Résolution des équations d'Euler par un schéma de Van Leer en éléments finis', *INRIA RR-358*, INRIA Sophia-Antipolis, 1985.
19. S. Lanteri, 'Simulation d'ecoulements, aérodynamicques instationnaires sur une architecture S.I.M.D. massivement parallèle', *Thèse de Doctorat en Sciences de l'Ingénieur*, Université de Nice-Sophia-Antipolis, 1991.
20. S. Piperno, 'Staggered time-integration methods for a one-dimensional Euler aeroelastic problem', *Rap. Rech. CERMICS 94-33*, 1994.
21. M. Lesoinne and C. Farhat, 'Geometric conservation laws for flow problems with moving boundaries and deformable meshes, and their impact on aeroelastic computations', *Comput. Meth. Appl. Mech. Engng.*, **134**, 71–90 (1996).

